SCIENTIFIC REPORTS
nature research

Check for updates

OPEN

High-performance thermochromic VO_2-based coatings with a low transition temperature deposited on glass by a scalable technique

David Kolenatý, Jaroslav Vlček✉, Tomáš Bárta, Jiří Rezek, Jiří Houška & Stanislav Haviar

We report on high-performance thermochromic $ZrO_2/V_{0.982}W_{0.018}O_2/ZrO_2$ coatings with a low transition temperature prepared on glass by a low-temperature scalable deposition technique. The $V_{0.982}W_{0.018}O_2$ layers were deposited by a controlled high-power impulse magnetron sputtering of V target, combined with a simultaneous pulsed DC magnetron sputtering of W target to reduce the transition temperature to 20–21 °C, at a low substrate surface temperature of 330 °C in an argon–oxygen gas mixture. ZrO_2 antireflection layers both below and above the thermochromic $V_{0.982}W_{0.018}O_2$ layers were deposited at a low substrate temperature (< 100 °C). A coating design utilizing a second-order interference in the ZrO_2 layers was applied to increase both the luminous transmittance (T_{lum}) and the modulation of the solar transmittance (ΔT_{sol}). The $ZrO_2/V_{0.982}W_{0.018}O_2/ZrO_2$ coatings exhibit T_{lum} up to 60% at ΔT_{sol} close to 6% for a $V_{0.982}W_{0.018}O_2$ thickness of 45 nm, and T_{lum} up to 50% at ΔT_{sol} above 10% for a $V_{0.982}W_{0.018}O_2$ thickness of 69 nm.

Vanadium dioxide (VO_2) undergoes a reversible phase transition from a low-temperature monoclinic VO_2(M1) semiconductive phase to a high-temperature tetragonal VO_2(R) metallic phase at a transition temperature (T_{tr}) of approximately 68 °C for the bulk material[1,2]. The abrupt decrease of infrared transmittance without attenuation of luminous transmittance in the metallic state makes VO_2-based coatings a promising candidate for thermochromic smart windows reducing the energy consumption of buildings. In spite of recent significant progress in fabrication and performance of thermochromic VO_2-based materials (see, for example, reviews[3–8] and the works cited therein), there are still serious drawbacks hindering their application in smart windows. These are: a high temperature needed for fabrication, a high transition temperature, a low luminous transmittance (T_{lum}), a low modulation of the solar transmittance (ΔT_{sol}) and low environmental stability. To meet the requirement for large-scale implementation on building glass, VO_2-based coatings should satisfy the following criteria simultaneously: deposition temperature close to 300 °C or lower[9–13], T_{tr} close to 20 °C[14], $T_{lum} > 60\%$[3,15,16], $\Delta T_{sol} > 10\%$[17–19], and long-time environmental stability[8,20–22].

Decrease of the deposition temperature of thermochromic VO_2-based coatings to 300 °C is of key importance: (1) to facilitate their large-scale production by reducing the energy consumption, simplifying substrate heating and cooling procedures and minimizing problems with a temperature non-uniformity over large substrate surfaces, and (2) to allow deposition of these coatings onto temperature-sensitive flexible substrates.

Magnetron sputter deposition with its versatility and the ease of scaling up to large substrate sizes is probably the most important preparation technique of thermochromic VO_2-based coatings[8,12,13]. In our recent works[23,24], reactive high-power impulse magnetron sputtering (HiPIMS) with an effective pulsed oxygen flow control (applicable to large-area coaters[25]) was used for low-temperature (300 °C) deposition of thermochromic VO_2 films onto conventional soda-lime glass without any substrate bias voltage and without any interlayer. Except for the work[11] with the same substrate surface temperature $T_s = 300$ °C, there is no work in the literature reporting a magnetron sputter deposition of thermochromic VO_2 films onto unbiased amorphous substrates at $T_s < 400$ °C[23,24]. The possibility to prepare thermochromic VO_2-based coatings without any substrate bias voltage is of key importance for their deposition on large area non-conductive (glass) substrates (no RF-induced bias needed). Here, it should

Department of Physics and NTIS – European Centre of Excellence, University of West Bohemia, Univerzitní 8, 306 14 Plzeň, Czech Republic. ✉email: vlcek@kfy.zcu.cz

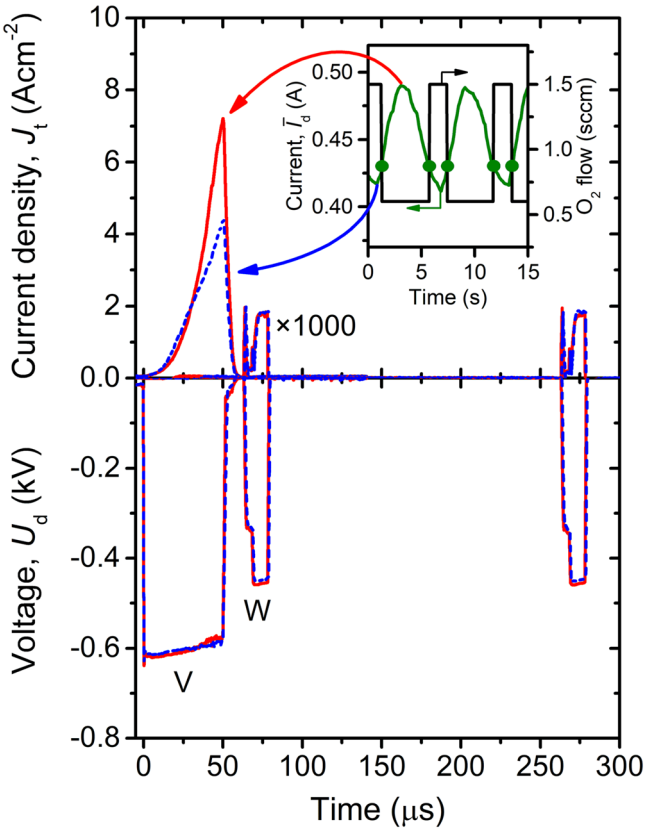

Figure 1. Waveforms of the magnetron voltage (U_d) and the target current density (J_t) for preset deposition-averaged target power densities of 12.9 W cm^{-2} and 33 mW cm^{-2} for V and W target, respectively, during a deposition of the $V_{0.982}W_{0.018}O_2$ films (the J_t values for W target are magnified 1,000 times). Time evolution of the average discharge current on V target in a period of the power supply ($\bar{I}_d$) during the deposition is shown in the inset. A pre-selected critical value $(\bar{I}_d)_{cr} = 0.43$ A determining the switch between the oxygen flow rates $\Phi_{ox} = 0.6$ sccm and $\Phi_{ox} = 1.5$ sccm is marked by dots. Reprinted from the work[28].

be mentioned that HiPIMS techniques are compatible with existing magnetron sputtering systems utilized in industrial deposition devices[26,27].

In this work, we report on high-performance three-layer thermochromic $ZrO_2/V_{0.982}W_{0.018}O_2/ZrO_2$ coatings with a low transition temperature (20–21 °C) prepared on soda-lime glass using a low-temperature (330 °C) magnetron sputter deposition without any substrate bias voltage. We present basic principles of this new solution for a low-temperature scalable deposition of high-performance durable thermochromic VO_2-based coatings for smart-window applications.

Methods

Coating preparation and elemental composition. The $V_{0.982}W_{0.018}O_2$ layers were deposited by controlled HiPIMS of V target, combined with a simultaneous pulsed DC magnetron sputtering of W target, at a low substrate surface temperature $T_s = 330$ °C and without any substrate bias voltage in an argon–oxygen gas mixture. The argon flow rate was 60 sccm corresponding to an argon partial pressure of 1 Pa, while the oxygen flow rate (Φ_{ox}) was not fixed but pulsing between 0.6 and 1.5 sccm (see Fig. 1), and the duration of the Φ_{ox} pulses (injecting oxygen in front of the sputtered V target toward the substrate[24]) was determined during the deposition by a programmable logic controller[29] using a pre-selected critical value of the average discharge current on V target in a period of the power supply $(\bar{I}_d)_{cr} = 0.43$ A. The basic principle of the pulsed oxygen flow control is illustrated in Fig. 1, which shows the time evolution of the magnetron voltage ($U_d(t)$) and the target current density ($J_t(t)$), averaged over the total target area, for both targets at the minimum and maximum value of the oxygen partial pressure in the vacuum chamber corresponding to the minimum and maximum $\bar{I}_d$, respectively, during the deposition. Here, it should be mentioned that the effective pulsed oxygen flow control makes it possible to utilize two benefits of the reactive HiPIMS deposition[23,24]. The first benefit is highly ionized fluxes of particles with many V^+ and V^{2+} ions onto the substrate and enhanced energies (up to 50 eV relative to ground potential) of the ions bombarding the growing films, allowing us to achieve the VO_2 crystallinity at a low T_s and without any substrate bias voltage. The second benefit is a very high degree of dissociation of the O_2 molecules injected into the high-density plasma in front of the V target, allowing us to achieve the required VO_2 stoichiometry at a

low compound fraction in the target surface layer. This is of key importance for reduced arcing, increased sputtering of V atoms, and low production of O^- ions at the target[29].

The depositions were performed in an ultra-high vacuum multi-magnetron sputter device (ATC 2200-V AJA International Inc.) using two unbalanced magnetrons with planar V and W targets (99.9% purity, diameter of 50 mm and thickness of 6 mm in both cases). The magnetron with a V target was driven by a high-power pulsed DC power supply (TruPlasma Highpulse 4002 TRUMPF Huettinger)[24]. The voltage pulse duration was 50 μs at a repetition frequency of 200 Hz (duty cycle of 1%) and the deposition-averaged target power density was 12.9 W cm^{-2}. The magnetron with a W target was driven by a pulsed DC power supply (IAP-1010 EN Technologies Inc.). The voltage pulse duration was 16 μs at a repetition frequency of 5 kHz (duty cycle of 8%) and the deposition-averaged target power density was 33 mW cm^{-2}. Under these conditions, the W content in the metal sublattice of $V_{1-x}W_xO_2$, as measured on a dedicated 285 nm thick film in a scanning electron microscope (SU-70, Hitachi) using wave-dispersive spectroscopy (Magnaray, Thermo Scientific), was 1.8 ± 0.6 at.% (i.e., $x = 0.018$).

Both bottom and top ZrO_2 antireflection layers were deposited by reactive mid-frequency AC magnetron sputtering without ohmic heating ($T_s < 100$ °C) and without any substrate bias voltage in an argon–oxygen gas mixture. The argon partial pressure was 1 Pa and the oxygen partial pressure was 0.35 Pa (oxide mode). The depositions were performed using two strongly unbalanced magnetrons with planar Zr targets (99.9% purity, diameter of 100 mm and thickness of 6 mm) driven by a mid-frequency AC power supply (TruPlasma MF 3010, TRUMPF Huettinger)[30]. The oscillation frequency was close to 85 kHz and the deposition-averaged target power density was 15.5 W cm^{-2}.

The thickness of individual layers was measured by spectroscopic ellipsometry using the J. A. Woollam Co. Inc. VASE instrument[31].

The presented deposition technique for preparation of the thermochromic $ZrO_2/V_{0.982}W_{0.018}O_2/ZrO_2$ coatings is, just like the deposition of low-emissivity coatings, compatible with the existing magnetron sputtering systems in glass production lines.

Coating structure and properties. For structural investigation of the films, X-ray diffraction (XRD) measurements were carried out using a PANalytical X´Pert PRO diffractometer working with a CuKα (40 kV, 40 mA) radiation at a glancing incidence of 1°. The average size of coherently diffracting regions of the VO_2(R)/VO_2(M1) phase was estimated from the full width at half maximum of the main VO_2(R)/VO_2(M1) diffraction peak, corrected for instrumental broadening, using the Scherrer's equation.

The surface morphology of the films was determined by atomic force microscopy (AFM) using a SmartSPM Microscope (AIST-NT) with a diamond tip (nominal radius below 10 nm) in a semicontact mode. The root-mean-square roughness of the surface, R_{rms}, was computed from a randomly selected square area of 1 × 1 μm^2. The AFM images were processed by Gwyddion 2.41 software[32], and an implemented "watershed" method was used for grain analysis. The grains identified were approximated by an equivalent disc diameter with the same projected area as the grain.

The hardness of VO_2 (without the ZrO_2 overlayer) was measured using a Hysitron TI 950 triboindenter with a cube corner tip at a maximum load of 100 μN.

The normal-incidence coating transmittance was measured by spectrophotometry using the Agilent CARY 7000 instrument equipped with an in-house made heat/cool cell. Spectroscopic measurements were performed in the wavelength range $\lambda = 300$ to 2,500 nm at the temperatures $T_{ms} = -5$ °C (semiconducting state below T_{tr}) and $T_{mm} = 60$ °C (metallic state above T_{tr}). Hysteresis curves were measured at $\lambda = 2{,}500$ nm in the temperature range $T_m = -10$ to 60 °C. The luminous transmittance (T_{lum}) and the solar transmittance (T_{sol}) are defined as follows

$$T_{lum}(T_m) = \frac{\int_{380}^{780} \varphi_{lum}(\lambda)\varphi_{sol}(\lambda)T(\lambda, T_m)d\lambda}{\int_{380}^{780} \varphi_{lum}(\lambda)\varphi_{sol}(\lambda)d\lambda}, \quad (1)$$

$$T_{sol}(T_m) = \frac{\int_{300}^{2500} \varphi_{sol}(\lambda)T(\lambda, T_m)d\lambda}{\int_{300}^{2500} \varphi_{sol}(\lambda)d\lambda}, \quad (2)$$

where φ_{lum} is the luminous sensitivity of the human eye and φ_{sol} is the sea-level solar irradiance spectrum[33] at an air mass of 1.5. The modulation of the luminous transmittance (ΔT_{lum}) and of the solar transmittance (ΔT_{sol}) are defined as

$$\Delta T_{lum} = T_{lum}(T_{ms}) - T_{lum}(T_{mm}), \quad (3)$$

$$\Delta T_{sol} = T_{sol}(T_{ms}) - T_{sol}(T_{mm}). \quad (4)$$

Using relation (2) it can be written

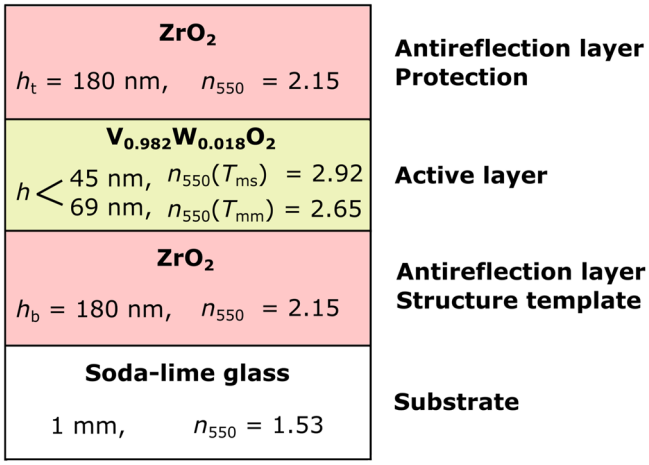

Figure 2. The three-layer thermochromic VO_2-based coating on a soda-lime glass substrate investigated in this paper. Here, h_b, h, and h_t represent the thickness of the bottom ZrO_2 layer, the thickness of the active $V_{0.982}W_{0.018}O_2$ layer, and the thickness of the top ZrO_2 layer, respectively. Below, individual coatings are referred to as (h_b, h, h_t). The refractive index (n_{550}) at the wavelength of 550 nm of all layers is also given. T_{ms} and T_{mm} denote the temperatures when the $V_{0.982}W_{0.018}O_2$ layer is in the semiconductive (below T_{tr}) and metallic (above T_{tr}) state, respectively. Reprinted from the work[28].

$$\Delta T_{sol} = \frac{\int_{300}^{2500} \varphi_{sol}(\lambda)\Delta T(\lambda)d\lambda}{\int_{300}^{2500} \varphi_{sol}(\lambda)d\lambda}, \quad (5)$$

where $\Delta T(\lambda) = T(\lambda, T_{ms}) - T(\lambda, T_{mm})$ is the modulation of the transmittance at the wavelength λ. The average luminous transmittance (T_{lum}) is defined as $T_{lum} = [T_{lum}(T_{ms}) + T_{lum}(T_{mm})]/2$.

Results and discussion

Design and transition temperature of $ZrO_2/V_{0.982}W_{0.018}O_2/ZrO_2$ coatings. The three-layer structure of $ZrO_2/V_{0.982}W_{0.018}O_2/ZrO_2$ coatings, formed by an active layer in the middle and two antireflection (AR) layers, is shown in Fig. 2. Let us emphasize the combination of properties which makes ZrO_2 a proper candidate for the AR-layers. First, ZrO_2 has a refractive index (n) close to the required geometric mean of refractive indices of $V_{0.982}W_{0.018}O_2$ and glass (bottom AR-layer) or $V_{0.982}W_{0.018}O_2$ and air (top AR-layer). Second, ZrO_2 has almost zero extinction coefficient (k) for visible and infrared wavelengths (λ), allowing one to utilize higher-order AR-layers without concessions in terms of absorption. Third, crystalline structure of the bottom ZrO_2 layer can be achieved even at a low deposition temperature, which in turn improves the $V_{0.982}W_{0.018}O_2$ crystallinity and the process reproducibility. Fourth, ZrO_2 is a hard (for an oxide) and stable material, which allows the top AR-layer to provide a mechanical protection and environmental stability for the active $V_{0.982}W_{0.018}O_2$ layer. The hardness of ZrO_2 prepared by the present technique is 15–17 GPa[30], compared to the hardness of VO_2 of only 12 GPa. Note that ZrO_2 layers are being increasingly applied in architectural glass as a protective overcoat for advanced low-emissivity stacks[34]. These properties cannot be matched by many other potential or occasionally used AR-layer materials due to their, e.g., non-zero k (Cr_2O_3), lower hardness (SiO_2, Ta_2O_5), high deposition temperature of the hardest phase (α-Al_2O_3), too low n for the bottom AR-layer (SiO_2) or usable but too high n (rutile TiO_2).

We examined the effect of smoothly varied h_b and h_t in our recent work[31] and thereby identified the optimum value $h_b = h_t = 180$ nm leading to a second-order interference maximum of T_{lum} (consistently with the optimization of h_t in the work[35]). This choice constitutes a crucial part of the efforts to maximize T_{lum} and ΔT_{sol} (at a given h) in parallel: while the frequently used first-order AR-layers ($\lambda/4$-layers; see e.g. the work[36] for a first-order ZrO_2 AR-layer) lead to a high transmittance modulation only in the far infrared (where it is weighted by weak solar irradiance when calculating ΔT_{sol}), second-order AR-layers ($3\lambda/4$-layers) lead to a high transmittance modulation mainly in the near infrared (where it is weighted by much higher solar irradiance; see below for a graphical example). Furthermore, we use two different h values of 45 nm or 48 nm (leading to higher T_{lum}) and 69 nm (leading to higher ΔT_{sol}) in order to demonstrate the corresponding tradeoff. Here, it should be mentioned that the thickness of the $V_{0.982}W_{0.018}O_2$ layer deposited onto amorphous soda-lime glass was 48 nm while it was 45 nm for the same layer deposited using the same discharge conditions (Fig. 1) and deposition time onto the crystalline ZrO_2 layer. To avoid any changes in the composition of the $V_{0.982}W_{0.018}O_2$ layer, which would be caused mainly by a larger erosion of the V target (see the much higher power compared with the W target) in additional (much later) depositions, we used the original configurations of the thermochromic VO_2-based coatings with the slightly different $h = 45$ nm and 48 nm in this work. The aforementioned effect of the thicker $V_{0.982}W_{0.018}O_2$ layer with $h = 69$ nm is presented for two important configurations, denoted as (180, 69, 0) and (180, 69, 180).

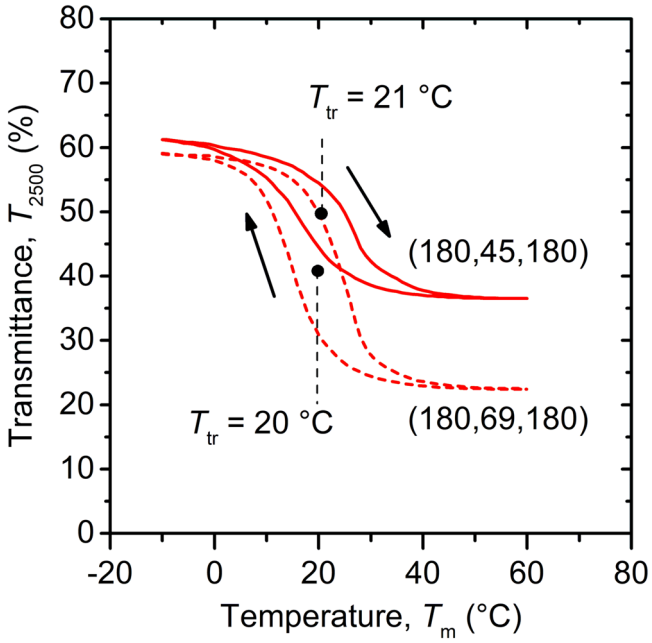

Figure 3. Temperature (T_m) dependence of the transmittance (T_{2500}) at 2,500 nm for the $ZrO_2/V_{0.982}W_{0.018}O_2/ZrO_2$ coatings with $h_b = 180$ nm, $h = 45$ nm or 69 nm, and $h_t = 180$ nm deposited onto 1 mm thick glass substrates (Fig. 2). The transition temperatures (T_{tr}) are also given. Adapted from the work.[28]

h (nm)	h_b (nm)	h_t (nm)	T_{tr} (°C)	T_{lum} (T_{ms}) (%)	T_{lum} (T_{mm}) (%)	ΔT_{lum} (%)	T_{sol} (T_{ms}) (%)	T_{sol} (T_{mm}) (%)	ΔT_{sol} (%)
48	0	0	23	33.5	35.5	−2.0	34.6	31.7	2.9
45	180	0	20	41.8	43.1	−1.3	40.4	36.1	4.3
69	180	0	19	38.6	36.6	2.1	34.4	26.3	8.1
48	0	180	25	54.3	53.5	0.8	46.3	41.8	4.5
45	180	180	21	59.7	59.1	0.6	49.9	44.4	5.5
69	180	180	20	49.9	46.0	3.9	42.4	32.0	10.4

Table 1. Thermochromic properties of different configurations of the VO_2-based coatings on 1 mm thick glass substrates. Here, h is the thickness of the $V_{0.982}W_{0.018}O_2$ layer, and h_b and h_t are thicknesses of the bottom and top ZrO_2 layers, respectively. Adapted from the work[28].

Figure 3 shows the dependence of the transmittance at $\lambda = 2{,}500$ nm (T_{2500}) on the measurement temperature (T_m) for two of the coatings prepared. The evaluated transition temperature (center of the hysteresis curves) was reduced by the aforementioned W doping to $T_{tr} = 20$–21 °C ($ZrO_2/V_{0.982}W_{0.018}O_2/ZrO_2$ coatings in Fig. 2) or 23 °C ($V_{0.982}W_{0.018}O_2$ without AR-layers in Table 1). The T_{tr} value is reproducible (almost the same for two different h values) and in agreement with the requirement for smart-window applications[14]. It is very important that using the present deposition technique, we did not experience any tradeoff (indicated in the literature[19,37,38]) between lowering T_{tr} by W doping and optimizing the other optical properties: the differences in the V(W)O_2 optical constants at $\lambda = 550$ nm were within the measurement error and reproducibility noise and did not exhibit any systematic dependence on the W content. The present W content of 1.8 ± 0.6 at.% and the transition temperature $T_{tr} = 57$ °C achieved for undoped VO_2 prepared by the same technique[23] collectively lead to a gradient of approximately (23–57)/1.8 = − 19 K/at.% of W in the metal sublattice, consistent with those (− 13 to − 22 K/at.%) reported in the literature[18,31,39].

Structure and morphology of $V_{0.982}W_{0.018}O_2$ layers. Figure 4 shows the coating structure at the temperature $T_m = 25$ °C, i.e., essentially during the thermochromic transition. The bottom ZrO_2 AR-layer [denoted as (180,0,0)] consists of a mixture of m-ZrO_2 (PDF#04-013-6875[40]) and t-ZrO_2 (PDF#01-081-1544 valid for $ZrO_{1.95}$). The strongest peaks around $2\Theta = 28.0°$ and 29.5° correspond well to the peaks of m-ZrO_2 [(− 111) planes diffracting at $2\Theta = 27.95°$] and t-ZrO_2 [(101) planes diffracting at $2\Theta = 29.81°$]. The $V_{0.982}W_{0.018}O_2$ layer with $T_{tr} = 23$ °C (Table 1) deposited onto glass [denoted as (0,48,0)] and the $V_{0.982}W_{0.018}O_2$ layer with $T_{tr} = 20$ °C deposited onto the crystalline ZrO_2 layer [denoted as (180,45,0)] consist of a mixture of the high- and low-temperature thermochromic phase, VO_2(R) (PDF#01-073-2362) and VO_2(M1) (PDF#04-003-2035), respectively, which are hard to distinguish. The strongest and sharp peak around $2\Theta = 27.8°$ corresponds well to the peaks

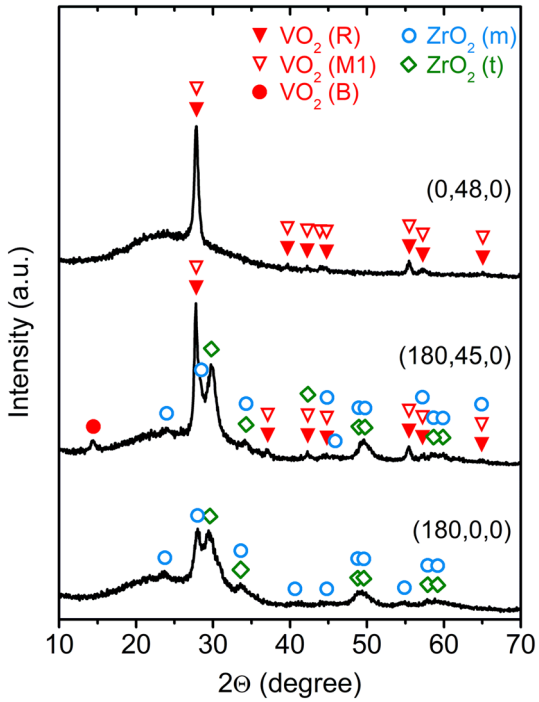

Figure 4. X-ray diffraction patterns taken at $T_m = 25$ °C from the $V_{0.982}W_{0.018}O_2$ layers with the thickness $h = 48$ nm deposited onto glass [denoted as (0,48,0)] and with the thickness $h = 45$ nm deposited under the same discharge conditions (Fig. 1) onto the ZrO_2 layer with the thickness $h_b = 180$ nm on glass [denoted as (180,45,0)]. For comparison, the X-ray diffraction pattern from the ZrO_2 layer with the thickness $h_b = 180$ nm on glass [denoted as (180,0,0)] is given. The main diffraction peaks of VO_2(R), VO_2(M1), VO_2(B), ZrO_2(m) and ZrO_2(t) are marked. Reprinted from the work[28].

of the VO_2(R), (110) planes diffracting at $2\Theta = 27.91°$, and the VO_2(M1), (011) planes diffracting at $2\Theta = 27.80°$. In spite of a small content of the non-thermochromic VO_2(B) phase (PDF#01-084-3056), the $V_{0.982}W_{0.018}O_2$ layer on the crystalline ZrO_2 layer exhibits a better crystallinity of the thermochromic VO_2(R)/VO_2(M1) phase. This is quantified in terms of larger size of the coherently diffracting regions, obtained using the peak around 27.8°. The size is 47 nm along the scattering vector (that is, for the 1° glancing incidence used, about $47 \cdot \cos[1° + 27.8°/2] = 45$ nm vertically, which is equal to the layer thickness) for the $V_{0.982}W_{0.018}O_2$ layer on ZrO_2, compared to 23 nm for the $V_{0.982}W_{0.018}O_2$ layer on glass.

The surface morphology of $V_{0.982}W_{0.018}O_2$ layers (without the top AR-layer) is shown in Fig. 5. The figure constitutes an independent confirmation of the fact that while the present deposition technique allows a low-temperature crystallization of VO_2-based layers on amorphous glass, their crystallinity on crystalline ZrO_2 is even better. Most importantly, the grains identified by the "watershed" method make up 80% of the projected surface area for the $V_{0.982}W_{0.018}O_2$ layer ($R_{rms} = 1.1$ nm) deposited onto the bare soda-lime glass (Fig. 5a), while they make up 94% of the projected surface area for the $V_{0.982}W_{0.018}O_2$ layer ($R_{rms} = 1.2$ nm) deposited onto the crystalline ZrO_2 AR-layer (Fig. 5b). Furthermore, the latter $V_{0.982}W_{0.018}O_2$ layer exhibits also a narrower distribution of the horizontal grain sizes (Fig. 5c).

Thermochromic properties of $ZrO_2/V_{0.982}W_{0.018}O_2/ZrO_2$ coatings. Figure 6 shows in detail the aforementioned role of second-order AR-layers in optimizing T_{lum} and ΔT_{sol}, given by Eqs. (1) and (5), respectively, in parallel. On the one hand, Fig. 6a,b show that T_{lum} depends only on a narrow range of wavelengths: the transmittance $T(\lambda, T_m)$ is weighted by a narrow function $\varphi_{lum}(\lambda)$. There is an easily explainable increase of $T(\lambda, T_m)$ in the corresponding narrow visible λ range, resulting from using only the bottom AR-layer, only the top AR-layer (stronger increase than the previous one) and both AR-layers (the strongest increase). This phenomenon is almost independent of T_m, which means that the low ΔT_{lum} (Table 1) is almost independent of the coating design. Furthermore, Fig. 6a,b confirm that owing to the absorption in $V_{0.982}W_{0.018}O_2$, $T(\lambda, T_m)$ is generally higher at $h = 45$ nm and 48 nm than at $h = 69$ nm.

On the other hand, Fig. 6c shows that the dependence of ΔT_{sol} on the coating configuration is much more difficult to explain, because the transmittance modulation $\Delta T(\lambda)$ is weighted by a wide and complicated function $\varphi_{sol}(\lambda)$ and there is no coating configuration leading to the highest $\Delta T(\lambda)$ in the whole λ range shown. Indeed, while $\Delta T(\lambda)$ in the far infrared above ≈1,600 nm (weighted by relatively low φ_{sol}) is actually the highest without any AR-layer, $\Delta T(\lambda)$ in the near infrared below ≈1,600 nm (weighted by relatively high φ_{sol}) is the highest when using both second-order AR-layers or at least the top one. The reason is that the second-order interference maxima on both AR-layers in the visible are followed by lower-order interference minima and maxima in the

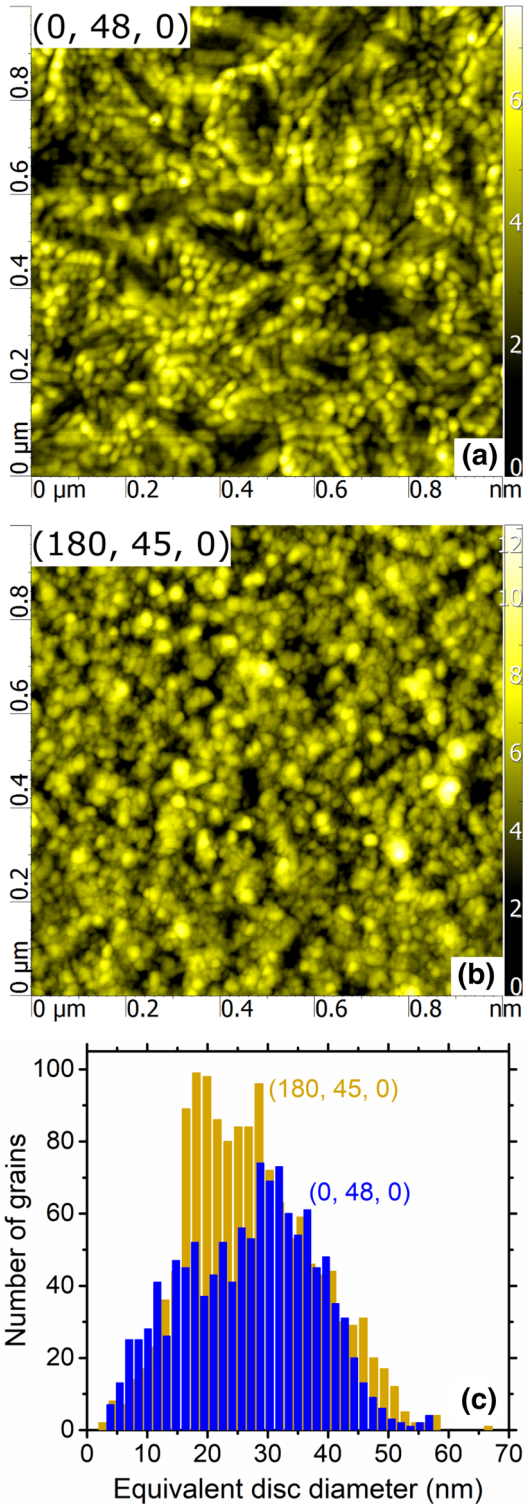

Figure 5. Surface morphology of the $V_{0.982}W_{0.018}O_2$ layers with the thickness $h = 48$ nm deposited onto glass [denoted as (0,48,0); panel **a**] and with the thickness $h = 45$ nm deposited onto the ZrO_2 layer with the thickness $h_b = 180$ nm on glass [denoted as (180,45,0); panel **b**], together with the corresponding grain-size (approximated by an equivalent disc diameter) distributions on the area of 1×1 µm^2; panel **c**. Reprinted from the work[28].

infrared, and that the overall improvement of the near infrared transmittance by this interference is more significant below than above T_{tr}. The fact that this kind of effect cannot be achieved by thinner first-order AR-layers

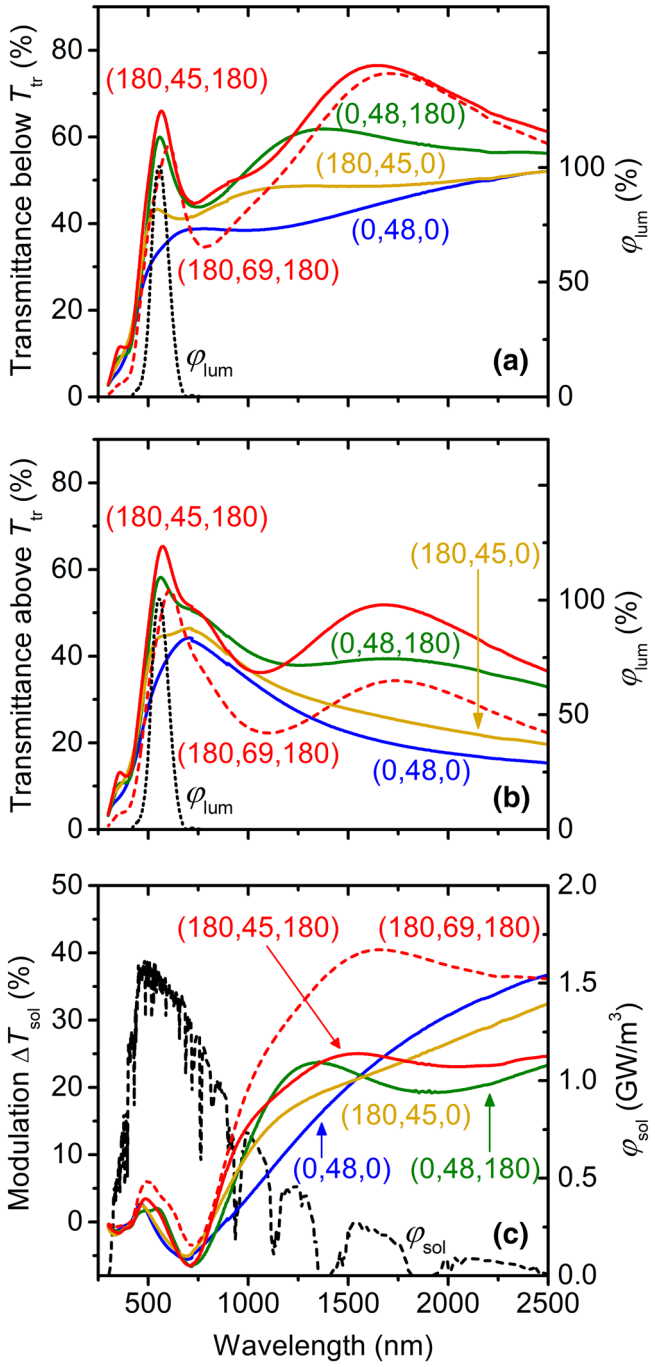

Figure 6. Spectral transmittance $T(\lambda, T_m)$ of different configurations (Table 1) of the thermochromic VO_2-based coatings on 1 mm thick glass substrates measured at $T_{ms} = -5$ °C (panel **a**) and $T_{mm} = 60$ °C (panel **b**), together with the corresponding modulation of the transmittance $\Delta T(\lambda)$; panel **c**. The coatings are denoted as (h_b, h, h_t), where h_b and h_t are the thicknesses of the bottom and top ZrO_2 layers, respectively. The thickness of the $V_{0.982}W_{0.018}O_2$ layer is $h = 45$ nm or 48 nm (solid lines) and $h = 69$ nm (dashed lines). The luminous sensitivity of the human eye (φ_{lum}) normalized to a maximum of 100%, and the sea-level solar irradiance spectrum (φ_{sol}) at an air mass of 1.5 are also given. Adapted from the work.[28]

is discussed in more detail in our recent work[31]. Furthermore, Fig. 6c confirms that $\Delta T(\lambda)$ is generally higher at $h = 69$ nm than at $h = 45$ nm or 48 nm.

The transmittance-based integral quantities, given by Eqs. (1)–(5), are summarized in Fig. 7 and Table 1. In agreement with the discussion of the transmittance in itself (Fig. 6), it can be seen that the transition from (1) bare $V_{0.982}W_{0.018}O_2$ through coatings with (2) only the bottom AR-layer and (3) only the top AR-layer to the coating with (4) both AR-layers, at almost the same thickness (45 nm and 48 nm) of the $V_{0.982}W_{0.018}O_2$ layer,

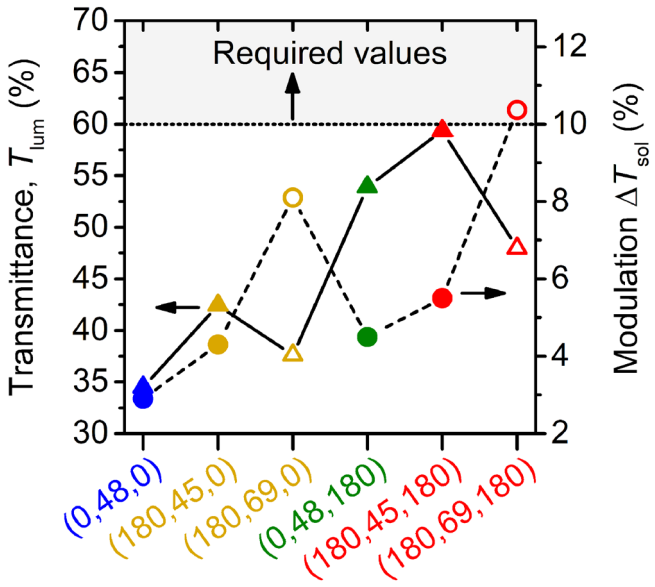

Figure 7. The average luminous transmittance (T_{lum}) and the modulation of the solar transmittance (ΔT_{sol}) for different configurations (Table 1) of the thermochromic VO_2-based coatings on 1 mm thick glass substrates. The coatings are denoted as (h_b, h, h_t), where h_b and h_t are thicknesses of the bottom and top ZrO_2 layers, respectively. The thickness of the $V_{0.982}W_{0.018}O_2$ layer is $h = 45$ nm or 48 nm (full symbols) and $h = 69$ nm (empty symbols). The gray region represents the required values for smart-window applications. Adapted from the work.[28]

$(T_s)_{max}$ (°C)	T_{tr} (°C)	T_{lum} (T_{ms}) (%)	T_{lum} (T_{mm}) (%)	ΔT_{sol} (%)	h (nm)	Preparation method	Refs.
Substrates: glass, silica* and fused quartz⁺							
330	20	49.9	46.0	10.4	69	HiPIMS + ACMS	This work
330	21	59.7	59.1	5.5	45	HiPIMS + ACMS	This work
330	40	43.9	40.0	11.6	76	HiPIMS + ACMS	31
400	32	60.9	65.0	3.6	Nanop.	Hydroth. + Anneal.	17
450	29	61.8	61.0	5.2	100	RFMS	18
450	34	36.2	32.3	14.6	145	DCMS + Anneal.	19
450	38	45.2	39.0	12.8	150	DCMS + Anneal.	37
500*	28	44.6	45.7	6.9	100	Sol–Gel + Anneal.	15
600⁺	35	71.6	70.1	8.6	392	Sol–Gel + Anneal.	41
Substrate: PET foils							
50	35	48.7	45.9	10.7	Nanop.	Hydroth. + Disper.	42
100	36	56.0	–	12.7	Nanop.	Hydroth. + Disper.	43

Table 2. Comparison between this work and previously reported studies on T_{lum} and ΔT_{sol} of VO_2-based coatings with a transition temperature $T_{tr} \leq 40$ °C prepared on glass substrates or polyethylene terephthalate (PET) foils. $(T_s)_{max}$ is the maximum substrate temperature during the preparation of the coatings and h is the thickness of the active VO_2-based layer. Here, ACMS, RFMS and DCMS denote the AC, RF and DC magnetron sputtering, respectively.

leads to a gradual improvement of the optical performance (average T_{lum} and ΔT_{sol}). The performance of the best coating configuration ($h_b = h_t = 180$ nm) is characterized by $T_{lum} = 59.4\%$ and $\Delta T_{sol} = 5.5\%$ (at $h = 45$ nm) and by $T_{lum} = 48.0\%$ and $\Delta T_{sol} = 10.4\%$ (at $h = 69$ nm), in both cases accompanied by low ΔT_{lum} and the aforementioned $T_{tr} = 20$–21 °C. It is possible to state that our results are close to the requirements (see the introductory part and the gray area in Fig. 7) for smart-window applications.

In addition to comparing the thermochromic properties of the present coatings with the industrial requirements, it is worth comparing them with the properties of coatings reported in the literature (Table 2). We focus on coatings on glass substrates and on plastic foils[42,43], which can be pasted on the glass, with an at least somewhat lowered $T_{tr} \leq 40$ °C.

The $ZrO_2/V_{0.988}W_{0.012}O_2/ZrO_2$ coating[31] was deposited using the same method as in the present work. The $V_{0.958}Tb_{0.031}W_{0.011}O_2$ coating[17] was fabricated on a glass substrate from Tb- and W-codoped VO_2 nanopowders

prepared using hydrothermal synthesis. An additional annealing at 400 °C for 60 min in argon atmosphere was ultimately applied to increase the adhesion and the coating crystallinity. The $V_{0.872}Sr_{0.119}W_{0.009}O_2$ layer, forming a basis for the $V_{0.872}Sr_{0.119}W_{0.009}O_2/SnO_2$ coating[18], was deposited by RF magnetron co-sputtering of V, Sr and W from a single composed V-Sr-W target in an argon–oxygen gas mixture at a substrate temperature of 450 °C. The $V_{0.931}Fe_{0.069}O_2$ coating[19] and $V_{0.878}Fe_{0.092}Mg_{0.030}O_2$ coating[37] were prepared by DC magnetron co-sputtering of V and Fe, and V, Fe and Mg, respectively, from a single composed V–Fe, and V–Fe–Mg target in an argon–oxygen gas mixture at a substrate temperature of 60 °C, with an additional in-situ annealing at 450 °C for 30 min in oxygen. The $V_{0.98}W_{0.02}O_2$ coating[15] was prepared on silica substrate by spin coating via a sol–gel process and annealing at 500 °C for 30 min in ammonia atmosphere. The $V_{0.99}W_{0.01}O_2$ coating[41] was prepared on fused quartz using a sol–gel method and annealing at 600 °C for 30 min in argon gas.

The thermochromic coatings, which were prepared on a polyethylene terephthalate (PET) substrate, are derived from $V_{0.971}F_{0.029}O_2$[42] or $V_{0.99}W_{0.01}O_2$[43] nanoparticles dispersed in polyurethane. These nanoparticles were produced by complex hydrothermal reactions. Here, it should be mentioned that the F-doping and W-doping of these nanoparticles resulted in the required reduction in the transition temperature, but it led also to a decrease in the modulation of the solar transmittance. The ΔT_{sol} value decreased from 13.1% for the coating with pure VO_2 nanoparticles to 10.7% (see Table 2) for the coating with 2.93 at.% F-doped VO_2 nanoparticles[42]. In case of the coating with 1 at.% W-doped VO_2 nanoparticles[43], the ΔT_{sol} value decreased to 12.7% (see Table 2) from 22.3% for the coating with pure VO_2 nanoparticles. Note that the transition temperature $T_{tr} = 36$ °C of the high-performance thermochromic coating with the $V_{0.99}W_{0.01}O_2$ nanoparticles (see Table 2) was determined as a mean value from the temperature of 46 °C, related to an endothermic peak, and 26 °C, related to an exothermic peak, detected using differential scanning calorimetry during the heating-up and cooling-down period, respectively.

As can be seen in Table 2, we achieved an excellent combination of the required characteristics: the lowest maximum glass temperature during the preparation of the coatings $(T_s)_{max} = 330$ °C, an appropriate transition temperature $T_{tr} = 20$–21 °C, and T_{lum} up to 60% at ΔT_{sol} close to 6% or T_{lum} up to 50% at ΔT_{sol} above 10%. These optical properties are comparable with those achieved for the thermochromic VO_2-based coatings which were prepared using long and too complicated chemical processes on flexible PET foils[42,43] at a very low $(T_s)_{max} \leq 100$ °C, but with too high transition temperatures $T_{tr} = 35$ °C and 36 °C, respectively.

Conclusion

High-performance thermochromic $ZrO_2/V_{0.982}W_{0.018}O_2/ZrO_2$ coatings with a low transition temperature were prepared on soda-lime glass by a low-temperature scalable deposition technique which is compatible with the existing magnetron sputtering systems in glass production lines. The $V_{0.982}W_{0.018}O_2$ layers were deposited by controlled HiPIMS of V target, combined with a simultaneous pulsed DC magnetron sputtering of W target (doping of VO_2 by W to reduce the transition temperature to $T_{tr} = 20$–21 °C without any degradation of thermochromic properties), at a low substrate surface temperature $T_s = 330$ °C in an argon–oxygen gas mixture. The effective pulsed oxygen flow control of the reactive HiPIMS deposition makes it possible to utilize the enhanced energies of the ions bombarding the growing $V_{0.982}W_{0.018}O_2$ layers for the support of the crystallization of the thermochromic VO_2 phase in them at the low $T_s = 330$ °C and without any substrate bias voltage. Our design of the three-layer VO_2-based coatings utilizes the second-order interference in two antireflection ZrO_2 layers to increase both the luminous transmittance and the modulation of the solar transmittance. The $ZrO_2/V_{0.982}W_{0.018}O_2/ZrO_2$ coatings exhibit the optical properties which are relatively close to the requirements ($T_{lum} > 60\%$ and $\Delta T_{sol} > 10\%$) for smart-window applications. For applications in large-scale systems, it is important that the presented controlled deposition of the active VO_2-based layers can be performed also at prolonged duty cycles (up to 5%). This results in up to 5 times lower target power density in a pulse at the same deposition-averaged target power density (approximately 13 W cm^{-2} in this work). Moreover, the deposition rate of these layers is higher.

Data availability

All experimental deposition conditions and characterization procedures, methods and data are provided in the text. Any clarifications will be available by contacting the corresponding author.

Received: 13 January 2020; Accepted: 22 May 2020
Published online: 06 July 2020

References

1. Morin, F. J. Oxides which show a metal-to-insulator transition at the Neel temperature. *Phys. Rev. Lett.* **3**, 34–36 (1959).
2. Wriedt, H. A. The O–V (oxygen–vanadium) system. *Bull. Alloy Phase Diagr.* **10**, 271–277 (1989).
3. Gao, Y. *et al.* Nanoceramic VO_2 thermochromic smart glass: a review on progress in solution processing. *Nano Energy* **1**, 221–246 (2012).
4. Granqvist, C. G. Recent progress in thermochromics and electrochromics: a brief survey. *Thin Solid Films* **614**, 90–96 (2016).
5. Wang, S. *et al.* Recent progress in VO_2 smart coatings: strategies to improve the thermochromic properties. *Prog. Mater. Sci.* **81**, 1–54 (2016).
6. Li, M., Magdassi, S., Gao, Y. & Long, Y. Hydrothermal synthesis of VO_2 polymorphs: advantages, challenges and prospects for the application of energy efficient smart windows. *Small* **13**, 1701147 (2017).
7. Xu, F., Cao, X., Luo, H. & Jin, P. Recent advances in VO_2-based thermochromic composites for smart windows. *J. Mater. Chem. C* **6**, 1903–1919 (2018).
8. Chang, T.-C. *et al.* Review on thermochromic vanadium dioxide based smart coatings: from lab to commercial application. *Adv. Manuf.* **6**, 1–19 (2018).
9. Fortier, J.-P., Baloukas, B., Zabeida, O., Klemberg-Sapieha, J. E. & Martinu, L. Thermochromic VO_2 thin films deposited by HiPIMS. *Sol. Energy Mater. Sol. Cells* **125**, 291–296 (2014).
10. Aijaz, A. *et al.* Low-temperature synthesis of thermochromic vanadium dioxide thin films by reactive high power impulse magnetron sputtering. *Sol. Energy Mater. Sol. Cells* **149**, 137–144 (2016).

11. Choi, Y., Jung, Y. & Kim, H. Low-temperature deposition of thermochromic VO_2 thin films on glass substrates. *Thin Solid Films* **615**, 437–445 (2016).
12. Sun, G. *et al.* Low-temperature deposition of VO_2 films with high crystalline degree by embedding multilayered structure. *Sol. Energy Mater. Sol. Cells* **161**, 70–76 (2017).
13. Chang, T. *et al.* Facile and low-temperature fabrication of thermochromic Cr_2O_3/VO_2 smart coatings: enhanced solar modulation ability, high luminous transmittance and UV-shielding function. *ACS Appl. Mater. Interfaces* **9**(31), 26029–26037 (2017).
14. Saeli, M., Piccirillo, C., Parkin, I. P., Binions, R. & Ridley, I. Energy modelling studies of thermochromic glazing. *Energy Build.* **42**, 1666–1673 (2010).
15. Hu, L. *et al.* Porous W-doped VO_2 films with simultaneously enhanced visible transparency and thermochromic properties. *J. Sol Gel Sci. Technol.* **77**, 85–93 (2015).
16. Baloukas, B., Loquai, S. & Martinu, L. VO_2-based thermally active low emissivity coatings. *Sol. Energy Mater. Sol. Cells* **183**, 25–33 (2018).
17. Wang, N., Goh, Q. S., Lee, P. L., Magdassi, S. & Long, Y. One-step hydrothermal synthesis of rare earth/W-codoped VO_2 nanoparticles: reduced phase transition temperature and improved thermochromic properties. *J. Alloys Compd.* **711**, 222–228 (2017).
18. Dietrich, M. K., Kuhl, F., Polity, A. & Klar, P. J. Optimizing thermochromic VO_2 by co-doping with W and Sr for smart window applications. *Appl. Phys. Lett.* **110**, 141907 (2017).
19. Lu, L. *et al.* Effect of Fe doping on thermochromic properties of VO_2 films. *J. Mater. Sci. Mater. Electron.* **29**, 5501–5508 (2018).
20. Loquai, S., Baloukas, B., Klemberg-Sapieha, J. E. & Martinu, L. HiPIMS-deposited thermochromic VO_2 films with high environmental stability. *Sol. Energy Mater. Sol. Cells* **160**, 217–224 (2017).
21. Chang, T. *et al.* Optical design and stability study for ultrahigh-performance and long-lived vanadium dioxide-based thermochromic coatings. *Nano Energy* **44**, 256–264 (2018).
22. Long, S. *et al.* Application-oriented VO_2 thermochromic coatings with composite structures: optimized optical performance and robust fatigue properties. *Sol. Energy Mater. Sol. Cells* **189**, 138–148 (2019).
23. Vlček, J., Kolenatý, D., Houška, J., Kozák, T. & Čerstvý, R. Controlled reactive HiPIMS—effective technique for low-temperature (300 °C) synthesis of VO_2 films with semiconductor-to-metal transition. *J. Phys. D: Appl. Phys.* **50**, 38LT01 (2017).
24. Vlček, J. *et al.* Ion-flux characteristics during low-temperature (300 °C) deposition of thermochromic VO_2 films using controlled reactive HiPIMS. *J. Phys. D: Appl. Phys.* **52**, 025205 (2019).
25. Bugyi, R., Vlcek, J., Rezek, J. & Lazar, J. High-rate reactive sputtering of dielectric stoichiometric films. Patent Nos. EP 2770083B1 (2015), US 9637814B2 (2017), CN 105264107B (2018), JP 6328150B2 (2018).
26. Gudmundsson, J. T., Brenning, N., Lundin, D. & Helmersson, U. High power impulse magnetron sputtering discharge. *J. Vac. Sci. Technol. A* **30**, 030801 (2012).
27. Gudmundsson, J. T. On reactive high power impulse magnetron sputtering. *Plasma Phys. Control. Fusion* **58**, 014002 (2015).
28. Kolenatý, D. *Low-temperature deposition of high-performance thermochromic VO_2-based coatings using pulsed reactive magnetron sputtering (Part G—draft of main results)*, Ph.D. Thesis, University of West Bohemia, Plzeň, Czech Republic (2018).
29. Vlček, J., Rezek, J., Houška, J., Kozák, T. & Kohout, J. Benefits of the controlled reactive high-power impulse magnetron sputtering of stoichiometric ZrO_2 films. *Vacuum* **114**, 131–141 (2015).
30. Rezek, J., Vlček, J., Houška, J., Čapek, J. & Baroch, P. Enhancement of the deposition rate in reactive mid-frequency ac magnetron sputtering of hard and optically transparent ZrO_2 films. *Surf. Coat. Technol.* **336**, 54–60 (2018).
31. Houska, J. *et al.* Significant improvement of the performance of $ZrO_2/V_{1-x}W_xO_2/ZrO_2$ thermochromic coatings by utilizing a second-order interference. *Sol. Energy Mater. Sol. Cells* **191**, 365–371 (2019).
32. Nečas, D. & Klapetek, P. Gwyddion: an open-source software for SPM data analysis. *Cent. Eur. J. Phys.* **10**, 181–188 (2012).
33. Available e.g. at https://rredc.nrel.gov/solar/spectra/am1.5/. https://hyperphysics.phy-astr.gsu.edu/hbase/vision/efficacy.html.
34. Oberste-Berghaus, J., Van Nuffel, R., Gobin, G., De Jaeger, K., Das, A. & De Bosscher, W. Film properties of zirconium oxide top layers from rotatable targets. In: *58th Annual Technical Conference Proceedings of SVC 2015*, pp. 228–234.
35. Chen, Z. *et al.* VO_2-based double-layered films for smart windows: optical design, all-solution preparation and improved properties. *Sol. Energy Mater. Sol. Cells* **95**, 2677–2684 (2011).
36. Xu, G., Jin, P., Tazawa, M. & Yoshimura, K. Optimization of antireflection coating for VO_2 based energy efficient window. *Sol. Energy Mater. Sol. Cells* **83**, 29–37 (2004).
37. Ji, C. *et al.* High thermochromic performance of Fe/Mg co-doped VO_2 thin films for smart window applications. *J. Mater. Chem. C* **00**, 1–3 (2018).
38. Zhang, J., He, H., Xie, Y. & Pan, B. Theoretical study on the tungsten-induced reduction of transition temperature and the degradation of optical properties for VO_2. *J. Chem. Phys.* **138**, 114705 (2013).
39. Romanyuk, A., Steiner, R., Marot, L. & Oelhafen, P. Temperature-induced metal-semiconductor transition in W-doped VO_2 films studied by photoelectron spectroscopy. *Sol. Energy Mater. Sol. Cells* **91**, 1831–1835 (2007).
40. JCPDS-ICDD, *PDF-4+ Database, International Centre for Diffraction Data*, Newton Square, PA, USA (2015).
41. Liang, Z. *et al.* Tungsten-doped vanadium dioxide thin films as smart windows with self-cleaning and energy-saving functions. *J. Alloys Compd.* **694**, 124–131 (2017).
42. Dai, L. *et al.* F-doped VO_2 nanoparticles for thermochromic energy-saving foils with modified color and enhanced solar-heat shielding ability. *Phys. Chem. Chem. Phys.* **15**, 11723–11729 (2013).
43. Chen, Z. *et al.* Fine crystalline VO_2 nanoparticles: synthesis, abnormal phase transition temperatures and excellent optical properties of a derived VO_2 nanocomposite foil. *J. Mat. Chem. A* **2**, 2718–2727 (2014).

Acknowledgements

This work was supported by the Czech Science Foundation under Project No. 17-08944S. The figures and tables used in this work have been adapted or reprinted from the Ph.D. Thesis of the first author[28].

Author contributions

J. V. directed this study. D. K., T. B. and J. R. prepared the samples. D. K. and T. B. carried out optical measurements. J. R. and S. H. analyzed the surface morphology and elemental composition of layers. All authors discussed the results. J. V., D. K. and J. H. wrote the manuscript.

Competing interests

The authors declare no competing interests.

Additional information

Correspondence and requests for materials should be addressed to J.V.

Reprints and permissions information is available at www.nature.com/reprints.